The Effects of Aggregation-Inducing Motifs on Amyloid Formation of Model Proteins Related to Neurodegenerative Diseases†

Motomasa Tanaka,‡ Yoko Machida,‡ Yukihiro Nishikawa,§ Takumi Akagi,⊥ Isao Morishima,|| Tsutomu Hashikawa,⊥ Tetsuro Fujisawa,§ and Nobuyuki Nukina*,‡

Laboratory for CAG Repeat Diseases, RIKEN Brain Science Institute, Saitama 351-0198, Japan, Laboratory for Structural Biology, RIKEN Harima Institute, Hyogo 679-5148, Japan, Laboratory for Neural Architecture, RIKEN Brain Science Institute, Saitama 351-0198, Japan, and Department of Molecular Engineering, Graduate School of Engineering, Kyoto University, Kyoto 606-8501, Japan

Received March 28, 2002; Revised Manuscript Received June 24, 2002

ABSTRACT: To examine the effects of aggregation-inducing motifs related to neurodegenerative diseases on amyloid formation of host protein, we prepared several chimera myoglobins, in which various aggregation-inducing motifs were inserted. The focused aggregation-inducing motifs included five (R5) or two (R2) oligopeptide repeats in yeast Sup35p, five octapeptide repeats (OPR) in the human prion protein, a nonamyloid β component (NAC) in α-synuclein, and tandem repeats of 50 glutamines (Q50). Circular dichroism and infrared spectroscopies suggested that the OPR, R5, and Q50 motifs formed an antiparallel β sheet as well as a random coil, whereas the R2 and NAC motifs mainly formed random coils. The OPR, R5, and Q50 mutants, but not the R2 and NAC mutants, readily formed the SDS-resistant aggregates under physiological condition, and electron microscopy revealed that the aggregates contained amyloid fibrils. The destabilization and increase in gyration radius of the OPR, R5, and Q50 mutants correlated with the tendency to form amyloid fibrils. A control mutant bearing a nonamyloidgenic sequence was also moderately destabilized but did not form amyloid fibrils. Therefore, we concluded that the OPR, R5, and Q50 motifs, even in a quite stable protein such as myoglobin, led the host protein to formation of amyloid fibrils under physiological condition.

Proteins normally function in natively folded states but continue to unfold and refold under certain conditions. When unfolded proteins refold, they occasionally undergo misfolding, which may generate stable insoluble aggregates. It has recently been reported that the deposition of such insoluble protein aggregates is associated with a range of human diseases, including CAG repeat diseases, Creutzfeldt−Jakob diseases, and Parkinson's disease. Although it is still debatable whether protein deposition is itself the primary origin of the pathological condition (*1*, *2*), a wide variety of experimental observations suggest that there is a strong causal link between the formation of aggregates and the onset of pathological symptoms (*3*). Interestingly, the causative proteins that form aggregates have no common properties with respect to function, amino acid sequence, or three-dimensional structure. However, most of the causative proteins include amino acid sequences that induce the formation of protein aggregates.

One of the best-characterized proteins carrying an aggregation-inducing motif is Sup35p in yeast. Sup35p is a translation termination factor known as a yeast prion due to its ability to convert normal phenotype of yeast to abnormal one. Liu and Lindquist have recently revealed that the prion conversion of Sup35p is modulated by the N-terminal five oligopeptide repeats with one partial imperfect repeat, PQGGYQQYN (*4*). In their study, a Sup35p mutant with two additional repeats induced a prion conversion significantly faster than the wild-type, whereas a Sup35p variant with only one repeat formed aggregates and underwent a prion conversion at a much slower rate than the wild-type. Thus, the five oligopeptide repeats in Sup35p are crucial for the formation of aggregates and prion conversion (*4*, *5*). The human prion protein (PrP)[1] also contains N-terminal five octapeptide (PHGGGWGQ) repeats similar to the five oligopeptide repeats in the N terminus of Sup35p. Expansion of the N-terminal repeats is found in certain families with inherited Gerstmann−Sträussler−Scheinker syndrome (GSS) and Creutzfeldt−Jakob disease, suggesting involvement of the octapeptide repeats in neuronal cell death (*6*). In transgenic mice expressing the repeat-truncated prion, prion

† This work was partly supported by grants-in-aid from the Ministry of Health and Welfare (N.N.) and from the Ministry of Education, Science, Sports and Culture of Japan (M.T., I.M., and N.N.).

* To whom correspondence should be addressed. Phone:+ 81-48-467-9702. Fax: +81-48-462-4796. E-mail: nukina@brain.riken.go.jp.

‡ Laboratory for CAG Repeat Diseases, RIKEN Brain Science Institute.

§ Laboratory for Structural Biology, RIKEN Harima Institute.

|| Department of Molecular Engineering, Kyoto University.

⊥ Laboratory for Neural Architecture, RIKEN Brain Science Institute.

[1] Abbreviations: PrP, prion protein; GSS, Gerstmann−Sträussler−Scheinker syndrome; NAC, nonamyloid β component; SW Mb, sperm whale myoglobin; OPR, octapeptide repeat in human PrP; R5, five oligopeptide repeat in Sup35p; MJD, Machado−Joseph disease; SAXS, small-angle X-ray scattering.

10.1021/bi0258905 CCC: $22.00
Published on Web 07/18/2002

titers, and levels of aggregated PrP have been shown to be lower than those in wild-type mice (*7*). In addition, the disease incubation time was increased, and there were no histopathological signs of scrapie infection in the brains of the transgenic mice, indicating that the octapeptide repeats have some effects on the formation of protein aggregates and propagation of prion (*7*). Apart from the oligopeptide repeats in Sup35p and human PrP, a tandem repeat of glutamine is also closely related to the formation of protein aggregates. The expansion of glutamine repeats to more than ~35−40 in causative proteins such as huntingtin induces the formation of intranuclear inclusions, which is the hallmark of polyglutamine diseases (*8*). The expanded polyglutamine recruits molecular chaperons and transcription factors to the protein aggregates, leading to the cellular dysfunction (*8*). Some of the amino acid sequences that do not include the repetitive sequences also facilitate the formation of protein aggregates. One of the best known sequences is the nonamyloid β component (NAC), which is composed of the amino acid residues from Glu61 to Val95 in α-synuclein. The NAC sequence has been reported to promote the formation of amyloid β aggregates (*9*) and form a core of α-synuclein aggregates that are major components of Lewy bodies found in patients of Parkinson's disease (*10*). Thus, the NAC sequence in α-synuclein is closely related to the protein deposition and neurodegeneration.

It should be noted here that the aggregation-inducing motifs are widely found in the proteins that cause neurodegenerative disorders but show a variety of amino acid sequences. The absence of sequence homology among aggregation-inducing motifs indicates that these motifs might be closely involved in inherent characteristics of their host proteins. Therefore, full characterization of the aggregation-inducing motifs will be crucial for a better understanding of the causative proteins and eventually the pathogenesis of the diseases. Since three-dimensional structures and stabilities of the host proteins that contain aggregation-inducing motifs are totally different, we cannot directly compare and evaluate the effects of the aggregation-inducing motifs on the structure and stability of their host proteins. To make such investigation possible, it is necessary to insert the aggregation-inducing motifs into the same protein. The chimera proteins harboring various aggregation-inducing motifs will allow us to examine and compare the effects of the aggregation-inducing motifs on their host proteins. These effects cannot be addressed by synthetic peptides of the aggregation-inducing motifs. Furthermore, structural analysis of the hybrid proteins will reveal structures of the aggregation-inducing motifs in protein, some of which remain controversial.

Since sperm whale myoglobin (SW Mb) shows remarkably high stability and solubility in water, we recently established the preparation of chimera Mbs with inserted glutamine repeats at the corner between the C and D helices (*11*). The previous study demonstrated that SW Mb is quite appropriate for a carrier protein of an aggregation-inducing domain. In the present study, we extended this strategy to other aggregation-inducing motifs related to neurodegenerative disorders. We focused on the five N-terminal octapeptide repeats (OPR) from Pro51 to Gln91 in human PrP, the five oligopeptide repeats (R5) from Pro41 to Asn93 in Sup35p, the NAC sequence from Glu61 to Val95 in α-synuclein as well as 50 glutamine repeats from the Machado-Joseph disease (MJD) protein. The initial two oligopeptide repeats from Pro41 to Asn64 in Sup35p (R2) were also introduced into Mb for comparison with the R5 motif. We inserted these aggregation-inducing motifs into the C−D corner of SW Mb and expressed the chimera Mb mutants, OPR, R2, R5, NAC, and Q50 Mbs in *Escherichia coli*, respectively. We also prepared a chimera myoglobin (C-term), in which a nonamyloidgenic sequence of the myoglobin C-terminal region (Leu104-Gly153) was inserted into the C−D corner. In the present study, we first examined the effects of these motifs on aggregate formation of the chimera Mbs and biochemical properties of the Mb aggregates. Next, we explored changes in protein stability and structure induced by the inserted motifs and investigated structural properties of the aggregation-inducing motifs, using various spectroscopies such as circular dichroism (CD), infrared (IR), and NMR.

EXPERIMENTAL PROCEDURES

Plasmid construction and protein expression. We amplified the DNA fragments of the aggregation-inducing and nonamyloidgenic sequences by PCR with human PrP, Sup35p, α-synuclein, MJD, and SW Mb genes. The DNA fragments of these motifs were ligated into the SpeI/PstI sites of the pUC19−SW Mb expression vector (*11*). The amino acid sequences of the inserted motifs are listed in Figure 1b. We added several amino acid residues from the original protein (human PrP, Sup35p, α-synuclein, and MJD) to both ends of the aggregation-inducing sequences as linkers in order to assist correct folding of the chimera Mbs.

TB1 was selected as a host *Escherichia coli* strain for expression of the pUC19−SW Mb vector. Recombinant SW Mb was expressed and purified as described previously (*12*). The concentration of ferric wild-type and mutant Mbs was determined by the extinction coefficient, 157 $mM^{-1}cm^{-1}$, at the Soret band in UV−visible spectra.

Characterization of Mb aggregates. To examine the formation of aggregates, we incubated 150 μM Mbs in 50 mM potassium phosphate buffer at pH 7.0 at 37 °C. At an appropriate time, 2 μL of the Mb solution was diluted to 100 μL of 50 mM potassium phosphate buffer at pH 7.0, and UV−visible spectra of the Mb solution were measured on a Shimadzu UV-2400 spectrophotometer. For the filter retardation assay, 150 μM Mb solution was first incubated for 5 days at 37 °C. A 1 μL sample of the Mb solution was diluted to 200 μL of 2% SDS solution and filtered on a BRL dot-blot filtration unit through a cellulose acetate membrane (0.2 μm pore size) that had been preequilibrated with 2% SDS (*13*). Filters were washed twice with 200 μL of 2% SDS and then blocked with 5% skim milk, followed by immunoblotting by polyclonal Mb antibody. For Congo red binding, 5 μL of the 150 μM Mb solution after 10-days incubation at 37 °C was added to 10 μM Congo red in 10 mM MOPS buffer (pH 7.0) and incubated at room temperature for 30 min. UV−visible spectra of the samples were measured using a Shimadzu 2400-PC. Congo red bound to fibril was determined using the equation: Congo red (mol/L) = $A_{540}/25\,295 - A_{480}/46\,306$ (*14*). For electron microscopy, 1 aliq. of 150 μM Mb solution after incubation at 37 °C for about 1 week was adsorbed onto carbon-coated 400-mesh copper grids and fixed by 2% paraformaldehyde−0.2%

(a)

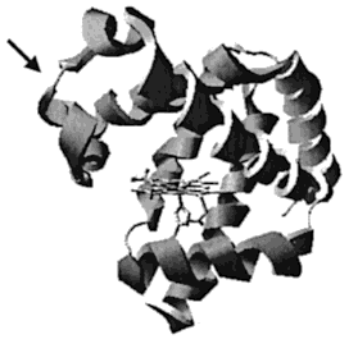

(b)

SWMb -----^{40}LEKFDRFKHLKTEAEM^{55}-----

LV ..... LQ

OPR	RYPPQ GGGGW GQ(PHGGGWGQ)$_4$ GGG
R2	QAQPA GGYYQ NYQGY SGYQQ GGYQQ YNPQG
R5	QAQPA GGYYQ NYQGY SGYQQ GGYQQ YNPDA GYQQQ YNPQG GYQQY NPQGG YQQQF NPQG
NAC	KTKEQ VTNVG GAVVT GVTAV AQKTV EGAGS IAAAT GFVKK D
Q50	YFEKQ QQK(Q)$_{50}$ RDLS
C-term	LEFIS EAIIH VLHSR HPGNP GADAQ GAMNK ALELF RKDIA AKYKE LGYQG

FIGURE 1: SW Mb mutants tethering inserted aggregation-inducing motifs as a model protein for neurodegenerative diseases. (a) X-ray crystal structure of SW Mb. The arrow indicates the C−D corner, into which various aggregation-inducing motifs were inserted; the stick model shows a heme prosthetic group. (b) Amino acid sequences inserted into the C−D corner of SW Mb.

glutaraldehyde in 100 mM sodium phosphate buffer. The sample was negatively stained with 2% sodium phosphotungstic acid. Images were recorded on a LEO 912AB electron microscope (LEO, Cambridge, U.K.) at a magnification of 63 000×.

Urea-induced unfolding experiments. To unfold Mb, we dissolved 2 μM Mb in 10 mM MOPS buffer containing 2 μM hemin and 80 μM KCN at 25.0 °C with various concentrations of urea (0−10 M). The reaction mixture was incubated at 25.0 °C for more than 1 h to reach equilibrium before acquiring CD or UV−visible spectra. Then we measured CD and UV−visible spectra of wild-type and mutant Mbs including various concentrations of urea and recorded the molar ellipticities at 222 nm and absorbances at 419 nm. The free energy of denaturation, ΔG, was calculated by the equation: $\Delta G = -RT \ln(f_D/(1 - f_D))$, where f_D is the fractional denatured population. When ΔG varies linearly with urea concentration, [urea], ΔG_{H_2O}, extrapolated ΔG at [urea] = 0, can be estimated by the following equation: $\Delta G = \Delta G_{H_2O} - m_{urea}$[urea], where m_{urea} is the slope of the linear relation between ΔG and [urea].

Spectroscopies. UV−visible spectra of ferric Mbs in 50 mM potassium phosphate buffer at pH 7.0 were recorded by a Shimadzu UV-2400 PC spectrophotometer (Shimadzu, Kyoto, Japan). The CD spectra of ferric Mbs (4.5 μM) in 50 mM potassium phosphate buffer, pH 7.0, were measured using a JASCO J-720 (Jasco Co., Tokyo, Japan) at 25 °C. The spectra were taken as the average of 16 scans recorded at a speed of 100 nm/min and a resolution of 0.2 nm. ^{1}H NMR spectra were acquired using a BRUKER Avance DRX600 spectrometer at 25.0 °C (Bruker, Rheinstetten, Germany). A LOSAT pulse sequence was employed with 64 000 data transformations of 180 kHz and a 14 μs 90° pulse (*15*). The concentrations of ferric and cyanide-ligated Mbs were approximately 400 and 200 μM, respectively, on the heme basis in 50 mM potassium phosphate buffer, pH 7.0, containing 90%H_2O/10%^2H_2O. Fourier-transferred infrared (FT-IR) spectra were measured on a TravelIR spectrophotometer (ST science, Tokyo, Japan). Approximately 1 mM solutions of ferric Mbs were prepared in 50 mM potassium phosphate buffer at pD 7.0. Deuterium oxide was used as the medium to improve the signal-to-noise ratio around 2100 cm^{-1}. FT-IR spectra of the ferric Mbs were taken as the average of 2048 or 4096 scans recorded at a speed of 30 scans/min and a resolution of 2 cm^{-1}. Spectral analysis by self-deconvolution was performed with Win-IR (Ver. 4.14J, BioRad).

Small-angle X-ray scattering (SAXS). SAXS experiments were carried out at RIKEN structural biology beamline BL45XU, SPring-8 in Harima, Japan (*16*). The sample-to-detector distance was about 2.2 m, which was calibrated with meridional diffraction of dried chicken collagen. Using an X-ray image intensifier and cooled CCD detector (XR-II + CCD) (*17*), each scattering profile was collected at room temperature for 1 s, during which no radiation damage was detected. The data were normalized to the intensity of the incident beam, and the buffer was subtracted. Protein concentration was varied from 1.2 to 2.2 mg/mL. The radius of gyration, R_g, was estimated by the Guinier approximation, $I(S) = I(0) \exp(-4\pi^2 R g^2 S^2/3)$, where S and $I(0)$ are the momentum transfer and intensity at the zero scattering angle, respectively, with fitting ranges of S^2 (Å^{-2}) from 5×10^{-6} to 25×10^{-6} (*18*). S is defined as $S = 2 \sin \theta/\lambda$, where 2θ and λ are the scattering angle and the X-ray wavelength, respectively. The distance distribution function, $P(r)$, was calculated by an indirect Fourier transform method of GNOM (*19*). The maximum dimension, D_{max}, was determined from the first zero cross-point of the $P(r)$ function (*18*).

RESULTS

Design and preparation of sperm whale myoglobin mutants. We prepared SW Mb mutants in which OPR, R2, R5, NAC, Q50, and C-term motifs were inserted at the C−D corner (Figure 1a). To facilitate the correct folding of the chimera Mbs and the formation of intrinsic structures of the inserted motifs, we added several residues from their original proteins as a linker to both ends of the inserted sequences, as illustrated in Figure 1b. Both mutant and wild-type Mbs were expressed in *Escherichia coli* and purified successfully. Isolation of the mutant Mbs was confirmed by immunoblotting with polyclonal antibodies for myoglobin, human PrP, and Sup35p NM domain (*20*) and with monoclonal antibodies for NAC (EQV-1) (*21*) and expanded polyglutamine (1C2) (*22*) (data not shown).

Formation and properties of aggregates in mutant Mbs. We examined the aggregate formation of the mutant Mbs

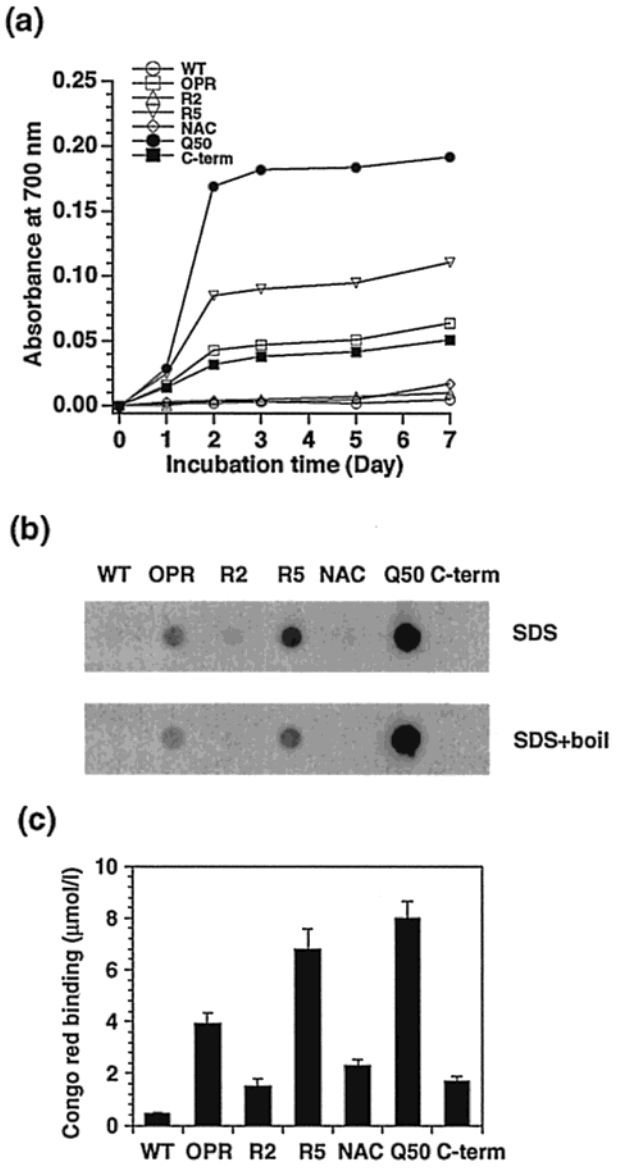

FIGURE 2: Properties of mutant Mb aggregates. 150 μM wild-type and mutant Mbs in 50 mM potassium phosphate buffer at pH 7.0 were incubated at 37 °C to estimate the formation rate and properties of aggregates. (a) Time-dependent aggregate formation. The turbidity of the Mb solution was monitored by an absorbance at 700 nm in UV−visible spectra. (b) SDS-resistant property of the Mb aggregates was examined by filter retardation assay. (c) The amount of Congo red (μmol/L) bound to amyloid fibrils. The values are the mean ± SEM.

under physiological condition. The mutant Mb solutions at pH 7.0 were incubated at 37 °C, and the formation of protein aggregates was estimated by the absorbance at 700 nm as the turbidity of the sample solutions (Figure 2a). Wild-type Mb was so stable that it formed no aggregates during the incubation. On the other hand, the R5 and Q50 mutants rapidly formed aggregates, while the OPR and C-term mutants also yielded aggregates, but at a more moderate rate. In contrast to these mutant Mbs, the R2 and NAC mutants formed aggregates very slowly, at a rate close to that for the wild-type Mb[2]. We found that the sample solutions of the aged R5 and Q50 mutants formed viscous gels and that the aged OPR sample also slightly exhibited the viscosity. However, we could not detect viscous gels in the sample solutions of the aged R2, NAC, and C-term mutants. To clarify biochemical properties of the aggregates, we first explored SDS resistance of the Mb aggregates by a filter retardation assay, using a polyclonal Mb antibody. The OPR, R5, and Q50 aggregates clearly showed a dot blot on the cellulose−acetate membrane, indicating that the aggregates of the OPR, R5, and Q50 mutants were resistant to SDS (Figure 2b). These aggregates were still resistant to SDS after boiling for 5 min. The intensity of the dot blot revealed that the Q50 aggregates showed the highest resistance to SDS, while the SDS resistance of the OPR aggregates was relatively mild. In contrast, we could not detect any positive dots for the aggregates of the R2, NAC, and C-term mutants, suggesting that these aggregates were susceptible to SDS. Next, we examined the binding of the Mb aggregates to Congo red, which is one of the standard tests to demonstrate the formation of amyloid fibrils. In this assay, we used the aggregates after 10-days incubation at 37 °C. The aggregates of the OPR, R5, and Q50 mutants showed high affinity for Congo red, whereas those of the R2, NAC, and C-term mutants did not (Figure 2c).

To confirm the formation of amyloid fibrils in the aggregates, we stained the aggregates of the mutant Mbs with 2% sodium phosphotungstic acid and observed them by electron microscopy (Figure 3). The Q50 mutant clearly formed amyloid fibrils with a diameter of 10−20 nm and length of 200−1000 nm, as reported previously (*11*). The R5 aggregates also contained fibrils similar to the Q50 fibrils, though the amount of R5 fibers was smaller than that of Q50 ones. Some of the amyloid filaments of the R5 and Q50 mutants twisted around each other to form helical structures, as shown in Figure 3. The OPR aggregates also contained fibrils, but the fibrils were thinner and shorter than those of the R5 and Q50 mutants. For the R2 and NAC aggregates, we observed a definite structure with a diameter of 10−20 nm and length of 50−100 nm. This morphology seemed to be quite different from the filamentous structure observed in the OPR, R5, and Q50 aggregates. The C-term mutant yielded only amorphous aggregates, which were clearly distinguished from those of the other mutant Mbs.

Effects of the aggregation-inducing motifs on protein stability. We carried out urea-induced denaturing experiments to investigate whether the aggregation-inducing motifs had any effect on the protein stability. The molar ellipticity at 222 nm and the absorbance at 419 nm (Soret maximum) correspond to the amount of α-helices and the extent of packing around the heme cofactor, respectively. Thus, we estimated the stabilities of α-helices and heme environmental structure in mutant Mbs by monitoring the molar ellipticity at 222 nm and the absorbance at 419 nm during unfolding of the wild-type and mutant Mbs, respectively. To follow the unfolding process precisely, we utilized the cyano forms of Mb, which avoid oligomerization of separated heme groups (*23*). In addition, we employed urea as a denaturant instead of guanidine hydrochloride, since guanidine hydrochloride was so strong that all mutant Mbs were severely destabilized even in a low concentration (data not shown).

[2] Addition of Q50 aggregates to the R2 and NAC mutant solutions (5% v/v) did not increase aggregate formation of the mutant Mbs. Seeding of R5 aggregates to the R2 sample (5% v/v) slightly accelerated aggregation of the mutant, whereas it did not have any effects on the NAC mutant.

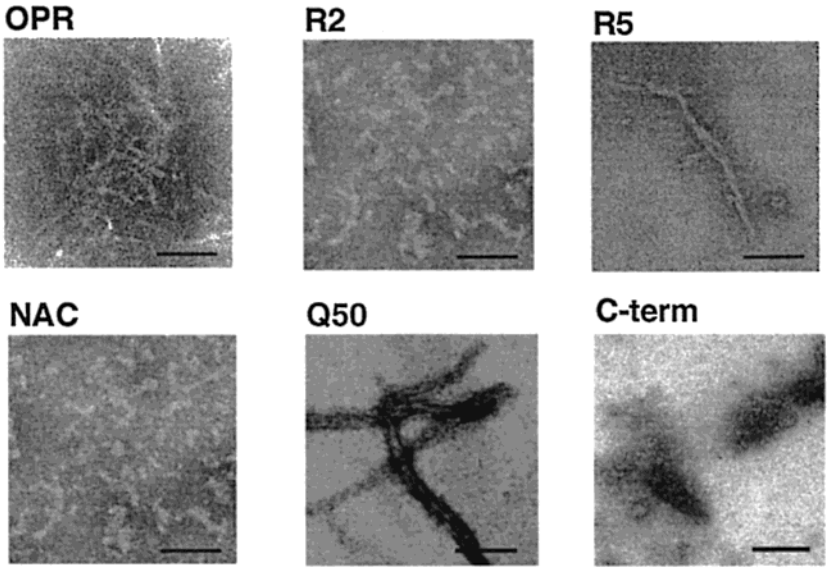

FIGURE 3: Morphology of the mutant Mb aggregates. Negative staining was performed with 2% sodium phosphotungstic acid and morphology of the aggregates was observed by electron microscopy. Scale bar, 100 nm.

Table 1: Stability Parameters Obtained by Urea-Induced Unfolding[a]

	CD (222 nm)		UV−visible (419 nm)	
Mbs	C_m (M)	ΔG_{H_2O} (kcal/mol)	C_m (M)	ΔG_{H_2O} (kcal/mol)
wild-type	8.7 ± 0.2	7.9 ± 0.3	8.4 ± 0.2	7.7 ± 0.3
OPR	4.5 ± 0.2	5.2 ± 0.3	4.7 ± 0.2	5.5 ± 0.2
R2	4.6 ± 0.1	6.7 ± 0.3	4.9 ± 0.1	6.0 ± 0.5
R5	4.2 ± 0.2	3.6 ± 0.4	4.1 ± 0.2	3.5 ± 0.4
NAC	4.6 ± 0.2	6.3 ± 0.3	4.8 ± 0.2	6.1 ± 0.2
Q50	4.2 ± 0.1	3.5 ± 0.4	4.3 ± 0.1	3.4 ± 0.4
C-term	4.5 ± 0.1	5.3 ± 0.4	4.7 ± 0.1	5.6 ± 0.3

[a] The values are the mean ± SEM.

The urea-induced unfolding curves of the wild-type and mutant cyanoMbs were monitored by molar ellipticity at 222 nm and absorbance at 419 nm. The unfolding curves showed the two-state transition under the present condition. From the sigmoidal curves, we calculated the concentration of urea at the midpoint of the unfolding transition (C_m) and the free energy of unfolding (ΔG_{H_2O}), both of which are the index of protein stability (*23*). These values were summarized in Table 1. C_m and ΔG_{H_2O} values calculated with both CD and UV−visible spectra were decreased in all mutant Mbs, indicating that all inserted motifs destabilized both of the α-helical packing and the heme environmental structure. We found that the R5 and Q50 mutants were most seriously destabilized and that the R2 and NAC mutants were relatively stable among mutant Mbs. The OPR and C-term mutants were also destabilized mildly, but the destabilization of these mutants was unambiguously small compared with that of the R5 and Q50 mutants.

Structural properties of the aggregation-inducing motifs in the mutant Mbs. We next investigated structural features of the inserted motifs related to neurodegenerative disorders. Secondary structures of the aggregation-inducing motifs in the mutant Mbs were first examined by circular dichroism (CD) spectroscopy. Figure 4a shows the CD spectra of the ferric wild-type and mutant Mbs in the far-UV region. The spectrum of the wild-type Mb, in which most of the amino acid residues constitute eight α-helices, was typical of an α-helical structure with two negative peaks at 208 and 220 nm (*24*). Although the spectral shapes of the mutant Mbs were similar to that of the wild-type Mb, negative molar ellipticities at 208 and 222 nm were enhanced in the OPR, R5, and Q50 mutants. Subtraction of the wild-type spectrum from the spectra of the Mb mutants delineated the CD spectra of the individual motifs introduced into Mb (Figure 4b). It is noticeable that all mutant Mbs showed a prominent decrease in the molar ellipticity at ∼200 nm. The difference spectra also indicated that insertion of the OPR, R5, and Q50 motifs diminished the molar ellipticities from 210 to 230 nm. Contrary to the OPR, R5, and Q50 motifs, the molar ellipticities in this region were not affected by insertion of the R2 and NAC motifs.

To examine the secondary structures of the aggregation-inducing motifs in more detail, we employed Fourier-transferred infrared (FT-IR) spectroscopy. The FT-IR spectra in the amide I region of wild-type and mutant Mbs are shown in Figure 5a. The major peak at 1650 cm^{-1} has been assigned to the amide I band of the α-helix (*25*), which is consistent with the fact that most of the amino acid residues constitute α-helices in SW Mb. Although the IR spectra of mutant Mbs closely resembled that of the wild-type, slight but significant differences were detected between wild-type and mutant Mbs. To clarify the spectral difference, we analyzed the IR spectra of wild-type and the mutant Mbs by self-deconvolution. The IR spectra were deconvoluted into the spectra with peaks at 1619 (turn or antiparallel β-sheet), 1625−30 (β-sheet), 1637 (solvated α-helix), 1643−46 (random coil), 1650−54 (α-helix), 1664 (turn), 1674 (turn), 1678 (turn), and/or 1685 (antiparallel β-sheet) cm^{-1} (*25*−*27*). However, this analysis was so sensitive to the number and peak positions of these components that we could not separate the spectra reproducibly and determine relative ratios of secondary structures exactly, probably due to presence of various states of secondary structures in the mutant Mbs. Instead, we could clearly extract the spectral differences by subtracting the spectrum of the wild-type from those of the mutant Mbs (Figure 5c, solid line). In the difference spectra, we observed two positive peaks at 1630 and ∼1675 cm^{-1},

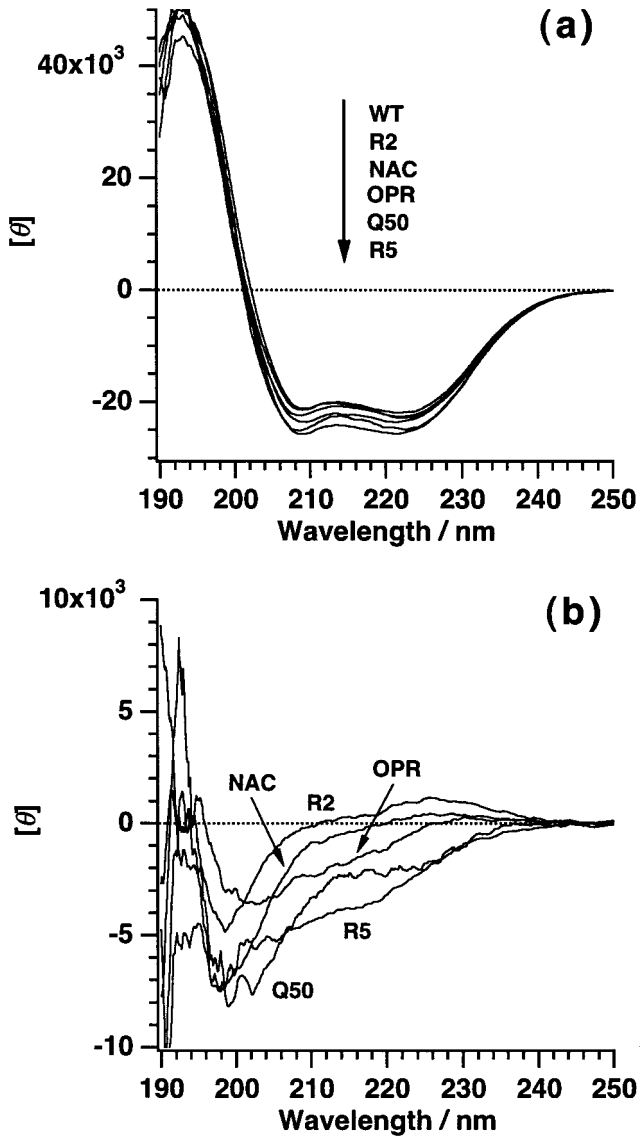

FIGURE 4: Secondary structure of mutant Mbs harboring the inserted aggregation-inducing motifs investigated by CD spectroscopy. (a) CD spectra of wild-type and mutant Mbs in the far-UV region. (b) Difference CD spectra obtained by subtracting the spectrum of wild-type from those of mutant Mbs.

and one negative peak at 1652 cm^{-1}. The positive peak at 1630 cm^{-1} is likely to include another peak at 1640 cm^{-1} as a shoulder. We also measured the IR spectra of the mutant Mbs that were incubated overnight at 37 °C (Figure 5b). We found some aggregates in the samples of the aged OPR, R5, and Q50 mutants. The difference IR spectra of the aged Mbs are shown by the dotted line in Figure 5c. A positive peak at 1630 cm^{-1} shifted to 1620 cm^{-1} in the difference spectra of the aged OPR, R5, and Q50 mutant Mbs. At the same time, a peak at ~1683 cm^{-1} was slightly but significantly enhanced in the difference spectra of these aged mutants. On the other hand, neither of the peaks at 1630 and 1683 cm^{-1} was observed in the aged R2 and NAC mutants (Figure 5c).

Structural effects of the aggregation-inducing motifs on the other regions of Mb. The preparation of the chimera Mbs prompted us to examine the structural effects of the inserted motifs on the host protein, Mb. We focused on conformational changes in the heme surroundings, which are buried into the Mb protein and distant from the insertion site on the protein surface. Since paramagnetic electrons of the heme-iron in Mb are very amenable to the electronic states of the heme and heme environmental structure (*28*), paramagnetic ^{1}H NMR spectra of the wild-type and mutant Mbs were used to clarify structural effects of the aggregation-inducing motifs on the heme and heme surroundings in the vicinity of the protein core. The resonances for heme peripheral methyl groups (8-, 5-, 3-, and 1-methyl group) and for $N_\delta H$ of the proximal His (His93) were observed at 90, 84, 72, 53, and 103 ppm, respectively, in the spectrum of ferric wild-type Mb, as reported previously (*29*). We measured paramagnetic ^{1}H NMR spectra of ferric mutant Mbs and found that the resonance positions in the low field did not change significantly by the insertions of the aggregation-inducing sequences, as shown in Figure 6a. This result was supported by UV−visible spectra of wild-type and mutant Mbs. The UV−visible spectra of all ferric mutant Mbs showed a strong peak at 408 nm (Soret band) and two minor peaks at 501 and 632 nm, which were almost identical to that of wild-type Mb (408, 502, and 633 nm) (data not shown).

To further explore heme environmental structures of the mutant Mbs, we measured ^{1}H NMR spectra of cyanide-ligated Mbs, in which several amino acid protons surrounding the heme group as well as heme peripheral protons have already been assigned in the low-field region. In the present study, the amino acid protons of His93 $N_\delta H$, Phe43 $C_\zeta H$, and His93 $N_p H$ were observed at 21.3, 17.2, and 13.8 ppm in the spectrum of the cyanide-ligated wild-type Mb, respectively (Figure 6b) (*30*). 5-, 1-, and 8-methyl protons of the heme group were also detected at 27.3, 18.7, and 12.9 ppm, respectively (*30*). We found that spectral profiles in the low field were not greatly affected by the aggregation-inducing domains, though the resonance position of 5-methyl protons of the heme showed a slight downfield shift by 1.7 ppm. In the high-field region, a broad signal at −9.9 ppm, which is assigned to Ile99 $C_\gamma H$, was also unaffected by the various insertions (data not shown) (*30*).

To gain further insights into structural effects of the aggregation-inducing motifs on the host protein, we examined the size of protein molecule by small-angle X-ray scattering using the beamline BL45XU at SPring-8 (*16*). The radius of gyration (R_g) and maximum dimension (D_{max}) of the wild-type and mutant Mbs[3] are summarized in Table 2. For purpose of comparison, the R_g and D_{max} values of the trichloroacetate-induced molten globule and urea-induced unfolded state are also listed (*31*). The R_g and D_{max} values of wild-type Mb were almost identical to those of a previous report (*31*). We found that the R_g and D_{max} of the mutant Mbs were augmented relative to those of wild-type Mb. Since the volumes of the mutant Mbs differed from that of the wild-type Mb due to insertion of the aggregation-inducing motifs, we calculated the expected R_g values of the mutant Mbs under the assumption that the volume was simply proportional to molecular weight (Table 2). The R5 and Q50 mutants showed larger R_g values than the expected ones. The

[3] An experiment by size exclusion chromatography revealed that OPR, R2, NAC, and Q50 mutant Mbs form only a monomer. However, the R5 mutant contained a small amount of oligomer, which would slightly increase the radius of gyration and the maximum dimension.

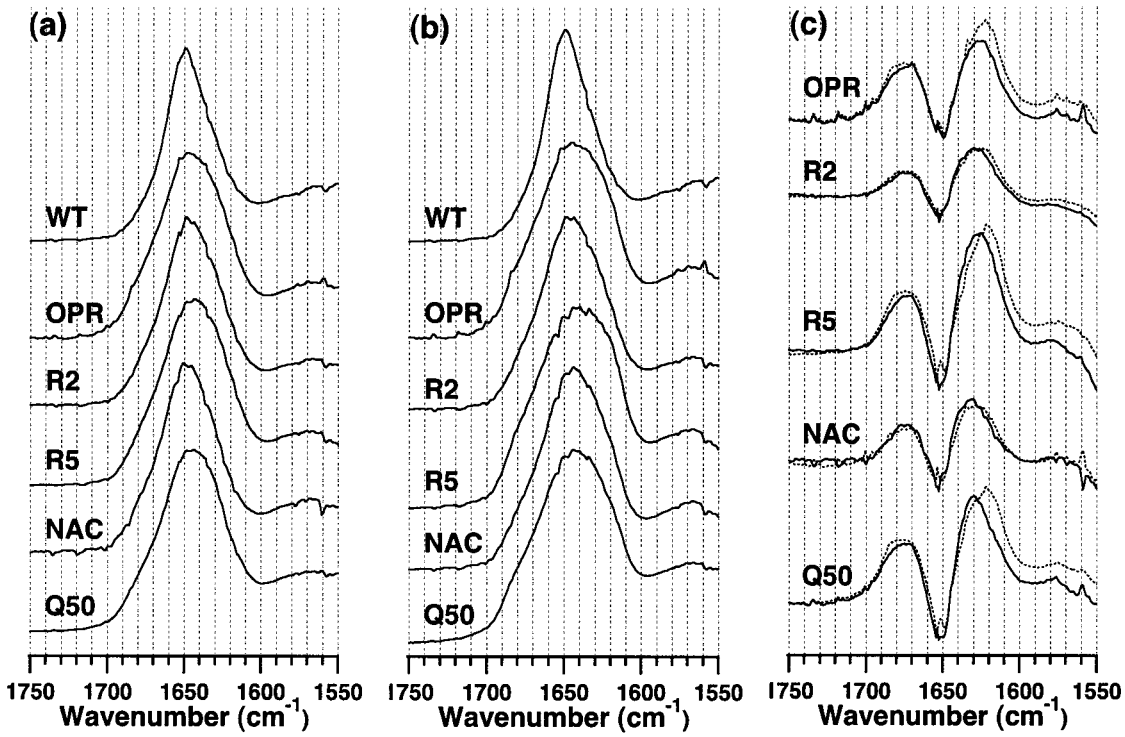

FIGURE 5: Secondary structure of mutant Mbs with inserted aggregation-inducing motifs investigated by IR spectroscopy. IR spectra of (a) soluble wild-type and mutant Mbs (b) wild-type and mutant Mbs after aging at 37 °C overnight in the amide I region. (c) Difference IR spectra were obtained by subtracting the IR spectrum of wild-type Mb from those of soluble (solid line) and aged (dotted line) samples of the mutant Mbs.

Table 2: Structural Parameters Obtained by SAXS for Wild-Type and Mutant Mbs[a]

myoglobins (molecular mass/Da)	R_g (Å)	expected R_g (Å)	D_{max} (Å)
wild-type (17 298)	17.4 ± 0.1	–	47.5 ± 2.5
OPR (21 165)	24.5 ± 0.5	18.6	82.5 ± 5.0
R2 (19 991)	20.9 ± 0.4	18.3	67.5 ± 2.5
R5 (23 339)	35.2 ± 1.1	19.2	100 ± 5.0
NAC (20 613)	21.9 ± 0.5	18.4	72.5 ± 2.5
Q50 (25 124)	27.2 ± 0.5	19.7	95.0 ± 5.0
molten globule[b]	23.1	–	72.5
unfolded state[c]	34.2	–	120

[a] The values are the mean ± SEM. [b] Trichloroacetate-induced molten globule (*31*). [c] Urea-induced unfolded state (*31*).

R_g value of the OPR mutant was smaller than those of the R5 and Q50 mutants but was apparently higher than the expected value. In contrast to the OPR, R5, and Q50 mutants, the increase in R_g was relatively small in the R2 and NAC mutants.

DISCUSSION

Secondary structures of the aggregation-inducing motifs in the mutant Mbs. We investigated the secondary structures of the aggregation-inducing motifs inserted in the chimera Mbs by comparing the spectra of the mutant Mbs with that of wild-type Mb. The presence of a random coil structure in all inserted aggregation-inducing motifs was indicated by the negative peak at 200−210 nm in the difference CD spectra and a positive peak at 1640 cm^{-1} as a shoulder in the difference IR spectra (*32*, *33*). In particular, the prominent negative peak at 200−210 nm in the difference CD spectra and the obvious shoulder peak at 1640 cm^{-1} in difference IR spectra of the R2 and NAC mutants indicated that random coils were more abundant in the R2 and NAC motifs. It has been reported that the NAC peptide in aqueous buffer forms a β-sheet structure, whereas its host protein, α-synuclein, forms a random coil (*34*). This fact together with our results suggested that the NAC motif introduced into a protein preferred a random coil to a β-sheet structure. In contrast to the R2 and NAC mutants, the molar ellipticities at 210−230 cm^{-1} in the difference CD spectra of the OPR, R5, and Q50 mutants suggested presence of a secondary structure in the OPR, R5, and Q50 motifs, though the secondary structure was obscure in the difference CD spectra. The strong positive peak at 1630 cm^{-1} in the difference IR spectra of the OPR, R5, and Q50 mutants revealed that an intramolecular β-sheet was formed in the OPR, R5, and Q50 motifs (*25*, *26*, *32*). The presence of a turn in the inserted motifs of the mutant Mbs was also indicated by the positive peak at ∼1675 cm^{-1} in the difference IR spectra (*25*, *26*, *32*). Since SW Mb does not contain any β-sheets, the simultaneous presence of a β-sheet and a turn suggested that the inserted OPR, R5, and Q50 motifs formed an antiparallel β-sheet. The pair of the peaks observed at 1620 and 1683 cm^{-1} in the difference IR spectra of the aged OPR, R5, and Q50 samples have been previously assigned to intermolecular antiparallel β-pleated sheets (*32*, *35*, *36*), supporting the presence of an intramolecular β-sheet in the OPR, R5, and Q50 motifs. While the β-sheet formation by an expanded polyglutamine was proposed previously (*37*, *38*), a solution structure of the R5 motif in Sup35p had not been solved. The β-sheet formation by the R5 motif in this study was supported by the recent X-ray crystal structure of the GNNQQNY peptide similar to the repetitive unit of the R5 motif (*39*). For the OPR motif, a synthetic peptide of OPR has been reported to adopt a β-turn structure, or a nonrandom and extended conformation

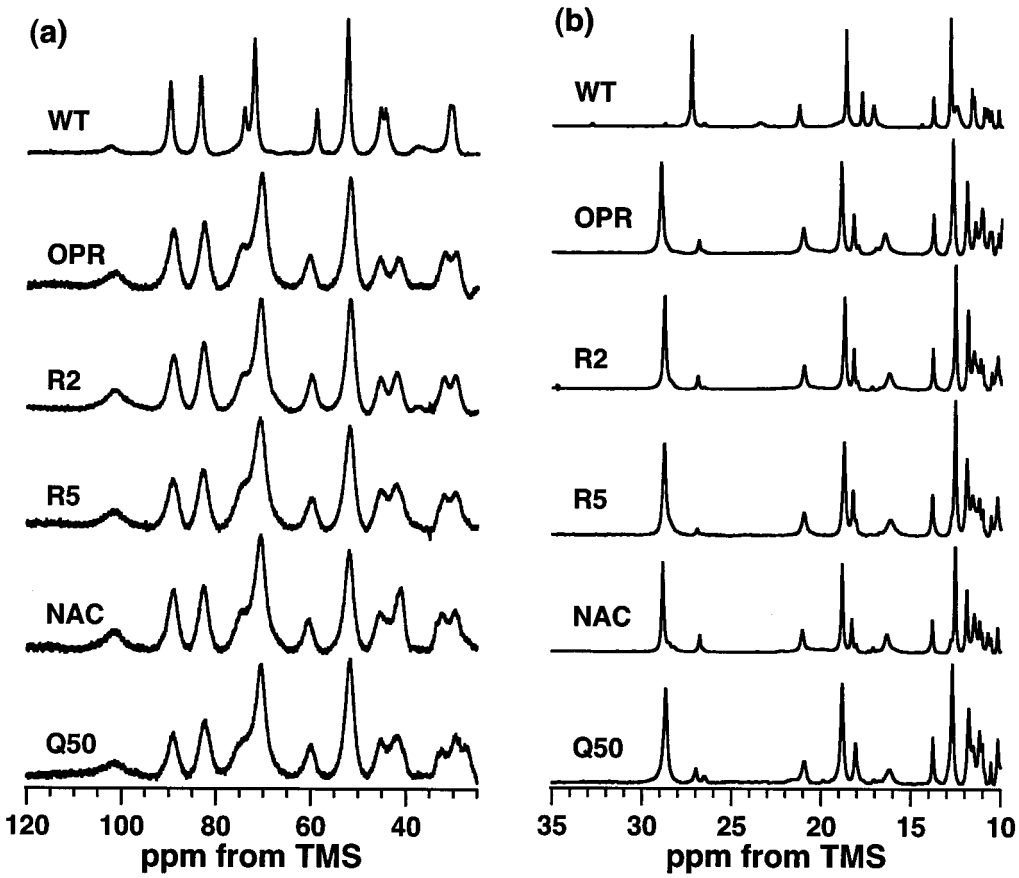

FIGURE 6: Small structural changes in the protein core by the aggregation-inducing motifs inserted into mutant Mbs. Paramagnetic ^{1}H NMR spectra of (a) ferric- and (b) cyanide-ligated forms of wild-type and mutant Mbs in 50 mM potassium phosphate buffer (pH 7.0) containing 90%H_2O/10%^2H_2O at 25.0 °C.

similar to a poly-L-proline type II left-handed helix (*40*, *41*). The former report agreed with our finding that OPR motif forms an antiparallel β-sheet as well as a random coil. Although the OPR, R5, and Q50 motifs formed an antiparallel β-sheet and a random coil, the variety of the difference CD and IR spectra of the OPR, R5, and Q50 mutants indicated that the relative ratios of the β-sheet, turn, and random coil structures are different between the OPR, R5, and Q50 motifs.

Properties of protein aggregates in the mutant Mbs. We also examined the effects of the aggregation-inducing motifs on protein aggregates. IR spectroscopy was applied to explore structures of the aggregates of the mutant Mbs. Since the pair of peaks at 1620 and 1683 cm^{-1} has been assigned to intermolecular antiparallel β-sheet aggregates (*32*, *36*), we revealed that the sample solutions of the aged OPR, R5, and Q50 mutants comprised amyloid fibrils composed of intermolecular antiparallel β-sheets. Although the C-term mutant harboring a nonamyloidgenic sequence also formed aggregates at a moderate rate, they were not amyloid fibrils but amorphous aggregates (Figures 2c and 3). The formation of amorphous aggregates in the C-term mutant was in accordance with their susceptibility to SDS (Figure 2b). These results suggested that the intramolecular β-sheet of the inserted OPR, R5, and Q50 motifs facilitated intermolecular interactions, resulting in formation of the amyloid fibrils constituted by antiparallel β-sheets.

We revealed that the aggregates of chimera Mbs showed different characteristic properties. The readily formation of SDS-resistant protein aggregates containing amyloid fibrils in the Q50 mutant was very similar to that seen in the GST-huntingtin fusion protein with a 51 glutamine repeat (*13*). The formation of SDS-resistant aggregates, including amyloid fibrils in the R5 mutant, also coincided with that observed in Sup35p (*42*). The SDS-resistance, number of amyloid fibrils, and viscosity of the solution indicated that the Q50 aggregates had properties more strongly indicative of amyloid fibrils than did the R5 aggregates. The relatively weak resistance to SDS and the fewer amyloid filaments in the R5 aggregates, compared with the Q50 aggregates, might be attributed to the absence of the Q/N-rich region of Sup35p in the inserted R5 motif. A previous study indicated that both of the Q/N-rich region and the R5 motif in the N terminus of Sup35p contribute to the formation of amyloid fibrils (*43*). The OPR mutant also yielded SDS-resistant aggregates containing amyloid fibrils, though amyloidogenic properties of the OPR aggregates were weaker than those of the Q50 and R5 aggregates (Figure 2b,c). The OPR motif, however, might not induce the aggregation of PrP in vivo because the octapeptide repeats in PrP are structurally fixed by their binding to copper ions (*44*). Nevertheless, the present results implied that the OPR motif facilitates the amyloid formation of PrP in GSS patients who have expanded octapeptide repeats in PrP, since the PrP in those patients contains free octapeptide repeats, as does the OPR mutant Mb. In fact, amyloid fibrils are observed in brain sections of the GSS patients having extra octapeptide repeats in PrP (*45*).

Although the amino acid sequence of the OPR motif is similar to that of the R5 motif, the OPR and R5 mutant Mbs yielded the protein aggregates with different properties. This study demonstrated that the subtle variance in amino acid sequence between OPR and R5 motifs induced the different properties of protein aggregates. The slow formation of aggregates and inability to form amyloid fibrils in the R2 mutant indicated that the whole repetitive sequence in the R5 motif is necessary to the rapid formation of aggregates containing amyloid fibrils. Our results using chimera Mbs agreed well with the previous report that the modulating repeat number in Sup35p alters the rate of protein aggregates (*4*). As observed for the R2 mutant, the NAC mutant also formed aggregates very slowly, suggesting that the NAC motif does not significantly induce the aggregate formation of its host protein. However, a recent study revealed that α-synuclein definitely forms amyloid filaments in vitro (*36*). While α-synuclein is abundant in random coils (*34*), the NAC mutant is rich in α-helices, and the protein molecule was relatively compact irrespective of the insertion of the NAC motif (Table 2). Therefore, the enhanced flexibility of the NAC motif in α-synuclein would accelerate the formation of amyloid fibers, compared with the NAC motif inserted into Mb. In other words, the originally partial unfolding would be an important factor to the amyloid formation in α-synuclein.

Effects of the aggregation-inducing motifs on host protein. It might be possible that the inserted motifs induced sufficient structural changes in the host protein for unfolding the protein and resulted in the formation of aggregates. Thus, we examined the effects of the aggregation-inducing motifs on the host protein, myoglobin. The insertion of the various aggregation-inducing motifs did not induce substantial changes in the profile of paramagnetic ^{1}H NMR spectra. Since paramagnetic ^{1}H NMR spectra are very amenable to subtle conformation of the heme group and heme surroundings that are buried in the protein (*28*), we concluded that structural changes in the vicinity of protein core, by insertion of the aggregation-inducing motifs, would be rather small. The slight negative peak at 1652 cm^{-1} in the difference IR spectra of the OPR, R5, and Q50 mutants suggested that most of α-helices in the mutant Mbs were formed as in the wild-type Mb. The SAXS experiments revealed an increase in gyration radius, especially in the OPR, R5, and Q50 mutants, relative to their expected radii (Table 2). These results implied that α-helices were not tightly packed in the OPR, R5, and Q50 mutants. This property−that secondary structures were formed but were partially packed−is typical of the molten globule state, which is observed as a folding intermediate. Therefore, the OPR, R5, and Q50 mutants might form a structure similar to the molten globule state. The larger R_g and D_{max} values of these mutant Mbs than those of the trichloroacetate-induced molten globule (Table 2) would be due to increase in the volume of the mutant Mbs by the large insert. The partial unfolding of the OPR, R5, and Q50 mutants correlated with the relatively large destabilization revealed by the urea-induced unfolding experiment (Table 1). The partial unfolding of the chimera Mbs would allow the aggregation-inducing motifs to fluctuate more freely, which facilitates the intermolecular interactions between aggregation-inducing motifs. Furthermore, hydrophobic residues exposed on protein surface upon partially unfolding might also participate in the intermolecular interactions because a partially unfolding apo-myoglobin from horse skeletal-muscle in pH 9.0 buffer at 65 °C has recently been shown to form amyloid fibrils (*46*). It is noticeable here that the C-term mutant, in which a nonamyloidgenic sequence was inserted, was moderately destabilized but did not form amyloid fibrils. These results revealed that an aggregation-inducing motif rather than partial unfolding plays major roles in the amyloid formation of the OPR, R5, and Q50 mutant Mbs.

In summary, we prepared and characterized chimera Mbs that contain various aggregation-inducing motifs. The OPR, R5, and Q50 mutants formed amyloid fibrils under physiological condition, whereas the R2 and NAC mutants did not. The partial destabilization and increase in gyration radius of protein molecule correlated with the aggregate formation in the OPR, R5, and Q50 mutants. The C-term mutant bearing a nonamyloidgenic sequence was also moderately destabilized but did not form amyloid fibrils. Therefore, we concluded that the OPR, R5, and Q50 motifs, even in a quite stable protein, led the host protein to formation of amyloid fibrils under physiological condition.

ACKNOWLEDGMENT

The authors thank Drs. T. Kitamoto (Tohoku University), J.S. Weissman (University of California, San Francisco), and K. Ueda (Tokyo Institute of Psychiatry) for the gifts of the plasmid vector encoding human PrP, a polyclonal Sup35p NM antibody, and a monoclonal EQV-1 antibody, respectively.

REFERENCES

1. Saudou, F., Finkbeiner, S., Devys, D., and Greenberg, M. E. (1998) *Cell 95*, 55−66.
2. Klement, I. A., Skinner, P. J., Kaytor, M. D., Yi, H., Hersch, S. M., Clark, H. B., Zoghbi, H. Y., and Orr, H. T. (1998) *Cell 95*, 41−53.
3. Davies, S. W., Turmaine, M., Cozens, B. A., DiFiglia, M., Sharp, A. H., Ross, C. A., Scherzinger, E., Wanker, E. E., Mangiarini, L., and Bates, G. P. (1997) *Cell 90*, 537−548.
4. Liu, J. J., and Lindquist, S. (1999) *Nature 400*, 573−576.
5. Li. L., and Lindquist, S. (2000) *Science 287*, 661−664.
6. Prusiner, S. B., and Scott, M. R. (1997) *Annu. Rev. Genet. 31*, 139−175.
7. Flechsig, E., Shmerling, D., Hegyi, I., Raeber, A. J., Fischer, M., Cozzio, A., von Mering, C., Aguzzi, A., and Weissmann, C. (2000) *Neuron 27*, 399−408.
8. Zoghbi, H. Y., and Orr, H. T. (2000) *Annu. Rev. Neurosci. 23*, 217−247.
9. Yoshimoto, M., Iwai, A., Kang, D., Otero, D. A., Xia, Y., and Saitoh, T. (1995) *Proc. Natl. Acad. Sci. U.S.A. 92*, 9141−9145.
10. Spillantini, M. G., Crowther, R. A., Jakes, R., Hasegawa, M., and Goedert, M. (1998) *Proc. Natl. Acad. Sci. U.S.A. 95*, 6469−6473.
11. Tanaka, M., Morishima, I., Akagi, T., Hashikawa, T., and Nukina, N. (2001) *J. Biol. Chem.* 276, 45470−45475.
12. Springer, B. A., and Sligar, S. G. (1987) *Proc. Natl. Acad. Sci. U.S.A. 84*, 8961−8965.
13. Scherzinger, E., Lurz, R., Turmaine, M., Mangiarini, L., Hollenbach, B., Hasenbank, R., Bates, G. P., Davies, S. W., Lehrach, H., and Wanker, E. E. (1997) *Cell 90*, 549−558.
14. Hartley, D. M., Walsh, D. M., Ye, C. P., Diehl, T., Vasquez, S., Vassilev, P. M., Teplow, D. B., and Selkoe, D. J. (1999) *J. Neurosci. 19*, 8876−8884.
15. Tanaka, M., Ishimori, K., and Morishima, I. (1998) *Biochemistry 37*, 2629−2638.
16. Fujisawa, T., Inoko, Y., and Yagi, N. (1999) *J. Synchrotron. Radiat. 6*, 1106−1114.
17. Ameyama, Y., Ito, K., Yagi, N., Asano, Y., Wakabayashi, K., Ueki, T., and Endo, T. (1995) *Rev. Sci. Instrum. 66*, 2290−2294.

18. Guinier, A., and Fournet, B. (1955) *Small-Angle Scattering of X-rays*, John Wiley, New York.
19. Svergun, D. I., Semenyuk, A. V., and Feigin, L. A. (1988) *Acta Crystallogr., Sect. A 44*, 244−250.
20. Sparrer, H. E., Santoso, A., Szoka, F. C., Jr., and Weissman, J. S. (2000) *Science 289*, 595−599.
21. Arima K., Ueda, K., Sunohara, N., Hirai, S., Izumiyama, Y., Tonozuka-Uehara, H., and Kawai, M. (1998) *Brain Res. 808*, 93−100.
22. Trottier, Y., Lutz, Y., Stevanin, G., Imbert, G., Devys, D., Cancel, G., Saudou, F., Weber, C., David, G., Tora, L., et al. (1995) *Nature 378*, 403−406.
23. Luo, Y., and Baldwin, R. L. (1998) *J. Mol. Biol. 279*, 49−57.
24. Townend, R., Kumosinski, T. F., Timasheff, S. N., Fasman, G. D., and Davidson, B. (1966) *Biochem. Biophys. Res. Commun. 23*, 163.
25. Dong, A., Huang, O., and Caughey, W. S. (1990) *Biochemistry 29*, 3303−3308.
26. Troullier, A., Reinstadler, D., Dupont, Y., Naumann, D., and Forge, V. (2000) *Nat. Struct. Biol. 7*, 78−86.
27. Williams, S., Causgrove, T. P., Gilmanshin, R., Fang, K. S., Callender, R. H., Woodruff, W. H., and Dyer, R. B. (1996) *Biochemistry 35*, 691−697.
28. Rajarathnam, K., La Mar, G. N., Chiu, M. L., Sligar, S. G., Singh, J. P., and Smith, K. M. (1991) *J. Am. Chem. Soc. 113*, 7886−7892.
29. La Mar, G. N., Budd, D. L., Smith, K. M., and Langry, K. C. (1980) *J. Am. Chem. Soc. 108*, 1822−1827.
30. La Mar, G. N., Emerson, S. D., Lecomte, J. T. J., Pande, U., Smith, K. M., Craig, G., and Kehres, L. A. (1986) *J. Am. Chem. Soc. 108*, 5568−5573.
31. Kataoka, M., Nishii, I., Fujisawa, T., Ueki, T., Tokunaga, F., and Goto, Y. (1995) *J. Mol. Biol. 249*, 215−228.
32. Dong, A., Matsuura, J., Manning, M. C., and Carpenter, J. F. (1998) *Arch. Biochem. Biophys. 355*, 275−81.
33. Townend, R., Kumosinski, T. F., Timasheff, S. N., Fasman, G. D., and Davidson, B. (1966) *Biochem. Biophys. Res. Commun. 23*, 163−169.
34. Weinreb, P. H., Zhen, W., Poon, A. W., Conway, K. A., and Lansbury, P. T., Jr. (1996) *Biochemistry 35*, 13709−13715.
35. Krimm, S., and Bandekar, J. (1986) *Advances in Protein Chemistry* (Anfinsen, C., Ed), 183−364.
36. Conway, K. A., Harper, J. D., and Lansbury, P. T., Jr. (2000) *Biochemistry 39*, 2552−2563.
37. Perutz, M. F., Johnson, T., Suzuki, M., and Finch, J. T. (1994) *Proc. Natl. Acad. Sci. U.S.A. 91*, 5355−5358.
38. Bevivino, A. E., and Loll, P. J. (2001) *Proc. Natl. Acad. Sci. U.S.A. 98*, 11955−11960.
39. Balbirnie, M., Grothe, R., and Eisenberg, D. S. (2001) *Proc. Natl. Acad. Sci. U.S.A. 98*, 2375−2380.
40. Smith, C. J., Drake, A. F., Banfield, B. A., Bloomberg, G. B., Palmer, M. S., Clarke, A. R., and Collinge, J. (1997) *FEBS Lett. 405*, 378−384.
41. Yoshida, H., Matsumoto N., Kumaki, Y., Nakata, M., and Hikichi, K. (2000) *J. Biochem. 128*, 271−281.
42. Glover, J. R., Kowal, A. S., Schirmer, E. C., Patino, M. M., Liu, J. J., and Lindquist, S. (1997) *Cell 89*, 811−819.
43. DePace, A. H., Santoso, A., Hillner, P., and Weissman, J. S. (1998) *Cell 93*, 1241−1252.
44. Brown, D. R., Qin, K., Herms, J. W., Madlung, A., Manson, J., Strome, R., Fraser, P. E., Kruck, T., von Bohlen, A., Schulz-Schaeffer, W., Giese, A., Westaway, D., and Kretzschmar, H. (1997) *Nature 390*, 684−687.
45. Goldfarb, L. G., Brown, P., Vrbovska, A., Baron, H., McCombie, W. R., Cathala, F., Gibbs, C. J., Jr., and Gajdusek, D. C. (1992) *J. Neurol. Sci. 111*, 189−194.
46. Frandrich, M., Fletcher, M. A., and Dobson, C. M. (2001) *Nature 410*, 165−166.

BI0258905